Please provide feedback
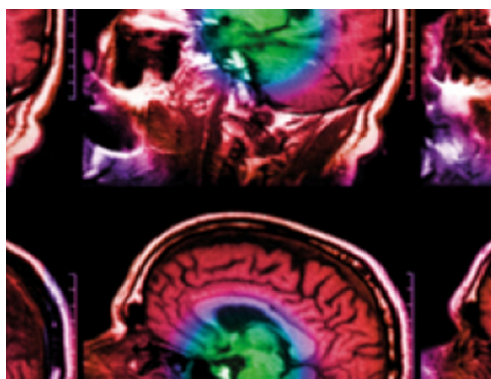
Please support the ScholarWorks@UMBC repository by emailing scholarworks-group@umbc.edu and telling us what having access to this work means to you and why it's important to you. Thank you.

PAPER

Pulsed focused ultrasound lowers interstitial fluid pressure and increases nanoparticle delivery and penetration in head and neck squamous cell carcinoma xenograft tumors

Physics in Medicine & Biology

PAPER

CrossMark

Pulsed focused ultrasound lowers interstitial fluid pressure and increases nanoparticle delivery and penetration in head and neck squamous cell carcinoma xenograft tumors

Ali Mohammadabadi[1,2], Ruby N Huynh[3] , Aniket S Wadajkar[4], Rena G Lapidus[5,6], Anthony J Kim[4,6,7], Christopher B Raub[3] and Victor Frenkel[1,6]

[1] Department of Diagnostic Radiology and Nuclear Medicine, University of Maryland School of Medicine, Baltimore, MD, United States of America
[2] Department of Mechanical Engineering, University of Maryland, Baltimore County, Catonsville, MD, United States of America
[3] Department of Biomedical Engineering, The Catholic University of America, Washington, DC, United States of America
[4] Department of Neurosurgery, University of Maryland School of Medicine, Baltimore, MD, United States of America
[5] Department of Medicine, University of Maryland School of Medicine, Baltimore, MD, United States of America
[6] University of Maryland Greenbaum Comprehensive Cancer Center, Baltimore, MD, United States of America
[7] Department of Pharmacology, University of Maryland School of Medicine, Baltimore, MD, United States of America

E-mail: vfrenkel@som.umaryland.edu

Abstract

Nanocarriers offer a promising approach to significantly improve therapeutic delivery to solid tumors as well as limit the side effects associated with anti-cancer agents. However, their relatively large size can negatively affect their ability to efficiently penetrate into more interior tumor regions, ultimately reducing therapeutic efficacy. Poor penetration of large agents such as nanocarriers is attributed to factors in the tumor microenvironment such as elevated interstitial fluid pressure (IFP) and fibrillar collagen in the extracellular matrix. Our previous studies reported that pretreatment of solid tumor xenografts with nondestructive pulsed focused ultrasound (pFUS) can improve the delivery and subsequent therapy of a variety of therapeutic formulations in different tumor models, where the results were associated with expanded extracellular spaces (ECS), an increase in hydraulic conductivity, and decrease in tissue stiffness. Here, we demonstrate the inverse relationship between IFP and the penetration of systemically administered nanoparticle (NP) probes, where IFP increased from the tumor periphery to their center. Furthermore, we show that pretreatment with pFUS can safely reduce IFP and improve NP delivery; especially into the center of the tumors. These results coincide with effects generated in the fibrillar collagen network microstructure in the ECS as determined by quantitative polarized light microscopy. Whole tumor and histomorphometric analysis, however, did not show significant differences in collagen area fraction or collagen feature solidity, as well as tumor cross-sectional area and aspect ratio, as a result of the treatments. We present a biophysical model connecting the experimental results, where pFUS-mediated cytoarchitectural changes are associated with improved redistribution of the interstitial fluid and lower IFP. The resulting improvement in NP delivery supports our previous therapeutic studies and may have implications for clinical applications to improve therapeutic outcomes in cancer therapy.

1. Introduction

Non-uniform and insufficient delivery of anti-cancer agents to solid tumors is a result of a number of well-identified factors in the tumor microenvironment (TME). These include abnormalities in the extracellular matrix (ECM) and the vasculature, leading to deficiencies in interstitial and transvascular transport, respectively, which can ultimately affect the bioavailability and efficacy of chemotherapeutic

agents (Galmarini and Galmarini 2003, Wang and Yuan 2006). Factors in the ECM of tumors can affect transport in the extracellular space (ECS), especially for larger agents (Wang and Yuan 2006). These include proteoglycans, collagen, and additional molecules, which are produced and assembled by stromal and tumor cells (Mow *et al* 1984, Mcguire *et al* 2006). An inverse relationship in tumors has been shown to exist between the amount of fibrillar collagen and interstitial diffusion of large macromolecules (Netti *et al* 2000) and oncolytic viruses (Mckee *et al* 2006). In the vasculature, leaky and immature blood vessels and a lack of functional lymphatics can lead to increases in the interstitial fluid pressure (IFP) in the TME (Mcdonald and Choyke 2003, Jain 2005). Increased IFP, which decreases the plasma to interstitial gradient, may severely limit extravasation of large, convection-dependent agents such as viral vectors and nanoparticle (NP)-based drug delivery platforms (Jain 2005, Di Paolo and Bocci 2007), reducing their penetration into tumors (Dreher *et al* 2006). High IFP, associated with poor delivery of therapeutics and treatment outcome, has been reported in solid tumors in both clinical (Gutmann *et al* 1992) and preclinical (Gutmann *et al* 1993, Winslow *et al* 2015) investigations.

Thermal ablation by focused ultrasound (FUS) is currently in use for the treatment of uterine fibroids and a variety of malignant tumors, including tumors in the breast, prostate and bone (Kennedy 2005, Focused Ultrasound Foundation). FUS for ablation is applied to elevate temperatures for destroying the tissue by the process of coagulative necrosis. FUS, provided using relatively short pulses (pFUS) and duty cycles, can substantially lower temporal averaged intensities, generating lower temperature elevations that do not create irreversible effects (Frenkel *et al* 2006, O'Neill *et al* 2009, Hancock *et al* 2009b). This allows for non-thermal mechanisms of ultrasound-tissue interactions to predominate, including those that can alter tissue cytoarchitecture and permeability for improving therapeutic delivery (Frenkel 2008a). Many of the investigations on pFUS-mediated delivery have been in the brain for opening the blood brain barrier (BBB) to improve the delivery of systemically administered agents. These treatments employ the administration of microbubbles (MBs, i.e. ultrasound contrast agents) that are activated by the varying pressure field of the pFUS exposures. The MBs are driven in to stable oscillations that can safely generate mechanical effects which have been shown to transiently increase the permeability of the BBB for facilitating delivery to the brain (Hynynen *et al* 2005, Chen *et al* 2013, Hersh *et al* 2016b).

In contrast to using pFUS to open the BBB, we have demonstrated how pFUS can be used to enhance the delivery of therapeutics in various solid tumor models. In human epidermoid xenograft tumors, we observed significantly enhanced delivery of a monoclonal antibody (mAb) labeled with ^{111}In when pretreating the tumors with pFUS compared to the agent on its own (Khaibullina *et al* 2008). A follow-up study with fluorescently labeled mAb showed pFUS to facilitate deeper penetration of the agent into the core of the tumors as well as further away from individual blood vessels. pFUS pretreatment and mAb labeled with Yettrium-90 (^{90}Y), resulted in slower tumor growth and greater survival of tumor bearing mice, compared to mAb treatment alone (Wang *et al* 2012). In studies in a murine model of head and neck squamous cell carcinoma (HNSCC), pFUS pretreatments were found to enhance the delivery of liposomal doxorubicin (Doxil®), a large molecular weight fluorophore (dextran-fluorescein, 500 kDa) (Yuh *et al* 2005), and plasmid encoding green fluorescent protein (GFP) (Dittmar *et al* 2005). Furthermore, we demonstrated how pFUS can improve the efficacy of the proteasome inhibitor, bortezomib (BTZ, Velcade®). When given twice weekly for two weeks, significant reductions in tumor growth were observed for a dose of 1 mg kg^{-1} with pFUS pre-treatment, being not significantly different than that achieved using a 50% increase (1.5 mg kg^{-1}) without pFUS (Poff *et al* 2008). In all studies, pFUS exposures alone were shown to be safe and did not affect tumor growth (Yuh *et al* 2005, Dittmar *et al* 2005, Frenkel *et al* 2006, Dromi *et al* 2007, Khaibullina *et al* 2008, Poff *et al* 2008, Hancock *et al* 2009a, Wang *et al* 2012, Ranjan *et al* 2012, Ziadloo *et al* 2013).

Strategies that provide well dispersed, sustained local drug concentrations in tumors could potentially improve the efficacy and reduce side effects of chemotherapy. In preclinical studies, for example, cisplatin-loaded liposomes were shown to lower IC$_{50}$ toxicity and improve treatment outcomes when combined with radiotherapy compared to free cisplatin (Harrington *et al* 2000a, 2000b). Cisplatin-loaded polymeric micelles were also shown to reduce nephrotoxicity and neurotoxicity compared to the free drug (Uchino *et al* 2005). In Phase I clinical trials for gastrointestinal tumors, these micelles also showed reduced cisplatin-related toxicity (Plummer *et al* 2011). Most NP-based drug formulations currently approved for cancer therapy exhibit limited tumor penetration due to binding to ECM molecules in the ECS, underscoring the need for strategies that enhance penetration within tumors following systemic administration. Our studies using NPs densely coated with polyethylene glycol (PEG) showed them to not adhere to biological tissues, including mucus, brain, and tumor tissue, thus allowing them to penetrate and distribute more uniformly *in vivo* (Nance *et al* 2012, Kim *et al* 2013, Schneider *et al* 2015). Using high-resolution, intravital microscopy in live mice, we showed PEG-coated NPs to penetrate significantly better in breast tumor xenografts, compared to uncoated NPs (Dancy *et al* 2016).

Despite the many advantages of nanocarriers for delivering therapeutics for the treatment of cancer, their relatively large size compared to the agents they encapsulate can mitigate their therapeutic advantage by negatively affecting their ability to efficiently extravasate and penetrate in the more interior regions of solid tumors, even when using PEG-coated NPs. These limitations have been attributed to factors in the TME (e.g. elevated levels of IFP and the presence of fibrillar collagen in the ECM) (Dewhirst and Secomb 2017). In this study, we demonstrate how pretreatment of tumors with pFUS can safely generate microarchitectural changes in the TME, where these were associated with a decrease in IFP and improved penetration and overall delivery of NP probes in the treated tumors. A biophysical model connecting the experimental results is proposed.

2. Materials and methods
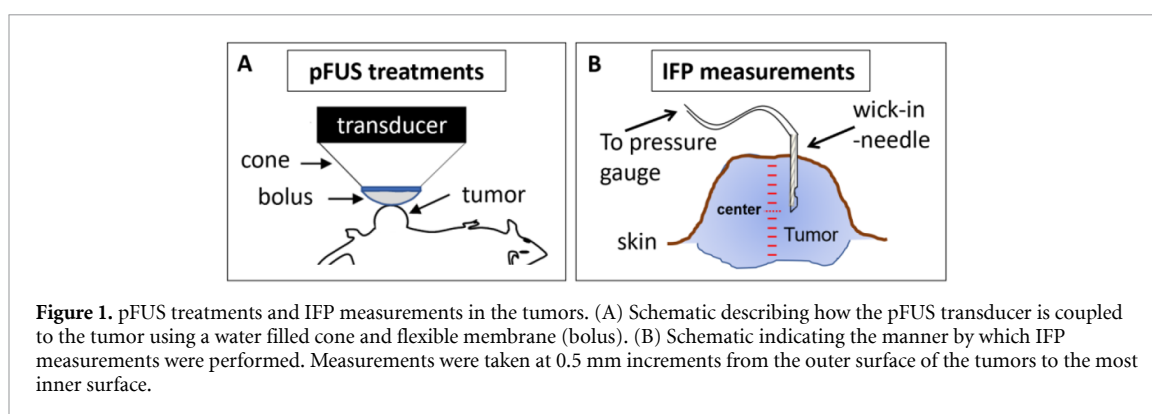
2.1. Animal and tumor model
All animal experiments were carried out according to an animal use protocol approved by the University of Maryland School of Medicine Institutional Animal Care and Use Committee (protocol #0717007). A FaDu HNSCC cell line (ATCC, HTB-43) and female athymic nude mice (Envigo RMS, Indianapolis, IN) were used for all experiments. The mice (~20 g) were socially housed in plastic bins with corn-cob bedding (24 cm × 19 cm × 18 cm) and received food and water ad libitum, with a room temperature of 23 °C and a 12 h light/dark cycle. Tumor cells (1×10^6) suspended in 70 μl of phosphate buffered saline (PBS) and 30 μl of Matrigel® were injected subcutaneously in the right flank of animals using a 26G needle and 1 ml syringe. Tumors were measured every 2 d. When they reached an approximate volume of 250 mm^3 they were randomized into the specific groups of the individual experiments. Note, the FaDu cells were authenticated by short tandem repeat analysis.

2.2. pFUS treatments
pFUS exposures were carried out using a custom FUS device (Anastasiadis *et al* 2019). The 500 kHz single element transducer (Sonic Concepts, Bothell, WA, USA) has a curvature radius of 63.2 mm and an aperture diameter of 82 mm (F-value = 0.77). The −6 dB beam size yields to a focal width of 2.36 mm and focal length of 13.50 mm. The transducer is driven by an acoustic amplifier (TPO-102, Sonic Concepts, Bothell WA, USA). And a clear plastic cone filled with degassed water facilitates coupling of the transducer to the tumor. The exit plane of the cone is sealed with an acoustically transparent (0.05″) silicone membrane (McMaster-Carr, Elmhurst, IL) (figure 1(A)). The height of coupling cone is 26.6 mm, which is the distance between the exit plane of the transducer housing to the exit plane of the cone. The center of focal zone (i.e. the location of peak pressure) occurs at 14.1 mm from the exit plane of the cone. Water is degassed using an in-line degassing membrane (PermSelect, Ann Arbor, MI, USA) powered by an external vacuum pump. The pFUS exposure were carried out at 80 W total acoustic power. With an average efficiency of 86%, the acoustic pressure at the center of focal zone was 5 MPa, corresponding to a spatial average, temporal peak (SATP) intensity of 1.55 kW cm^{-2}. For each treatment location, 10 ms bursts were provided at a 10% duty cycle. Exposures were rastered over the projected surface of the tumors at a 1.5 × 1.5 mm spacing, using a custom positioning system (Velmex, Bloomfield, NY, USA). The position of the focal zone in the *x–y* plane of the projected surface was determined using a custom laser-guidance apparatus (Anastasiadis *et al* 2019). 1200 individual pulses were given at each individual treatment location for a total treatment time per location of 120 s.

2.3. IFP measurements
Measurements of IFP were carried out using the wick-in-needle method as previously described (figure 1(b)) (Znati *et al* 1996, Elmghirbi *et al* 2018). Briefly, a 23-gauge (0.6 mm) needle with a 2 mm long side-port located 3 mm from the needle tip was connected to a 1 ml syringe. A polyester multifilament thread was inserted in the needle. A custom positioning system (Velmex, Bloomfield, NY, USA) was used for positioning the syringe and inserting the needle into the tumor. The syringe was connected to a TruWave pressure transducer (model PX12N; Edwards Lifesciences LLC, Irvine, CA) using 2 mm polyethylene tubing with a length of 20 cm. The needle and tubing were filled with PBS, and air bubbles were eliminated using Luer-Lock connections and syringes. The pressure transducer was connected to a strain gauge meter (model PAXLS; Red Lion Controls, York, PA). The measuring system was calibrated using a water column and values were translated from mm H$_2$O to mm Hg (1 mm Hg = 13.595 mm H$_2$O). The measurement procedure was carried out by inserting the needle at the outer surface of the tumor and taking measurements at a step size of 0.5 mm until reaching the inner surface of the tumor. Measurements were performed in control (n = 10) and immediately following pFUS treated tumors (n = 10).

Figure 1. pFUS treatments and IFP measurements in the tumors. (A) Schematic describing how the pFUS transducer is coupled to the tumor using a water filled cone and flexible membrane (bolus). (B) Schematic indicating the manner by which IFP measurements were performed. Measurements were taken at 0.5 mm increments from the outer surface of the tumors to the most inner surface.

2.4. NP preparation

Methoxy-PEG5k-amine was purchased from Creative PEGWorks (Winston Salem, NC). Red 40 nm (580ex/605em) and Dark Red 200 nm (660ex/680em) carboxyl-modified polystyrene (PS-COOH) FluoSpheres were purchased from Invitrogen (Carlsbad, CA). To formulate the PEG-coated NP probes, 40 and 200 nm PS-COOH NPs were covalently modified with methoxy-PEG5k-amine by carbodiimide chemistry as we previously described (Dancy *et al* 2016). After the reaction, particles were purified by centrifugation using Amicon Ultra-15 ml filters (100 kDa) with ultrapure water for a total of three washes. 40 and 200 nm PS-PEG NPs (0.5 mg ml^{-1}) were resuspended in ultrapure water and stored at 4 °C until use.

2.5. *In vivo* imaging of NP delivery

For the *in vivo* imaging study, all animals (n = 5 per group) were imaged together at 24 h following systemic administration (200 μl) via the tail vein of 40 nm PS-PEG NPs (0.5 mg/ml), with and without pFUS pretreatment. Injections in the pFUS group were given immediately following the treatments. Animals were imaged by the IVIS® Spectrum *in vivo* imaging system (Perkin Elmer, Akron, OH). A standard region of interest (ROI) was selected that best represented all the tumors' projected surface in the shape of an oval using the IVIS graphic user interface (height: 20 mm; width: 15 mm). The ovals were positioned over the tumors and the level of epifluorescence determined (excitation: 570 nm; emission: 600 nm; 5 s exposure). The imaging exposure time was determined so that the epifluorescence signal was below a saturation threshold for the brightest signal visualized for all the tumors of both groups imaged simultaneously, as standard procedure. Mean levels of epifluorescence in the tumors were calculated for each experimental group and compared.

2.6. Characterization of NP tumor penetration

For the study on characterizing the distribution and penetration of NPs in the tumor sections, animals (n = 7 per group) were euthanized at 24 h following systemic administration (200 μl) via the tail vein of 200 nm PS-PEG NPs (0.5 mg/ml), with and without pFUS pretreatment. Whole tumors were resected and preserved overnight in 2% PFA at 4 °C. Tumors were then embedded in 5% low melting point agarose gel and sectioned (200 μm slices) using an OTS-4000 vibratome (Electron Microscopy Sciences, Hatfield, PA). Sections (three per tumor at their maximum diameter, 200 μm thick) were mounted on glass slides and whole tumor digital images captured (excitation: 620; emission: 700 nm) using a BZ-X800 fluorescence imager (Keyence, Itasca, IL). Images were processed in ImageJ v1.52n (NIH) (Snipstad *et al* 2017) as follows. Individual tumor images were uploaded and converted from RGB to 8-bit grayscale using the 'type conversion' feature and binarized using the 'binary processing' feature. The 'Otsu' auto threshold algorithm was used for the binarization process. The 'line drawing' tool was then used to generate three exclusive ROIs. In 'freehand selection' mode the outer tumor border was outlined, excluding the skin, constituting the largest ROI. Inner ROIs, at 1/3 and 2/3 diameter of the outside tumor diameter, were generated using the 'reverse enlarging' feature. The 2/3 ROI did not include the 1/3 ROI. And the outer ROI similarly did not include the 2 interior ones. The mean signal intensity of the fluorescent signals (representing the NPs) within each ROI was determined using the 'analyze' feature. Values for each ROI, for control and pFUS treated tumors, were normalized to the total value for each tumor section to represent the relative value for each ROI. Mean values were first determined for each tumor (n = 3) and then used to determine mean values for each experimental group (n = 7) for comparison between the treatments.

2.7. Quantitative polarized light microscopy (qPLM) of tumor section birefringence

For the study on characterizing the effects of pFUS on fibrillar collagen, animals (n = 3) were euthanized immediately following pFUS treatments. A group of untreated animals (n = 3) was used as controls. Processed tumors were embedded in paraffin, sectioned, and stained with hemotoxylin and eosin (H&E) and Masson's Trichrome (MTC) by NDB Bio, LLC (Baltimore, MD). The collagen network microstructure in control and pFUS treated tumors was assessed using qPLM (Rieppo *et al* 2008, Li *et al* 2017). Briefly, the birefringence signal from unstained, deparaffinized slides of tumor sections was imaged using a polarized light microscope (MT9930, Meiji Techno, Ltd., Japan) in transmission mode, equipped with a green filter ($\lambda = 546$ nm), a linear polarizer and an analyzer positioned perpendicularly to the polarizer. The optical axis of each specimen was aligned by rotating the circular rotatable microscope stage until the brightest birefringence signal was observed. The polarizer and analyzer were both rotated in 15° increments up to 90°, maintaining their relative positions to each other. Seven images were captured at each rotation step. At 90° rotation, a quarter-wave plate (546 nm) was inserted into the illumination path after the analyzer, and two additional images were captured with the analyzer rotated ±1–5°, while keeping the polarizer at the same position. The maximum intensity polarized signal was obtained from a pixel-wise sinusoid least-squares fitting of co-registered images in MATLAB$^{\circledR}$ with an average 7% error. The theoretical maximum signal, I_{MAX} from each pixel was placed in a maximum signal intensity map and was independent of specimen orientation. These sections were compared to serially adjacent sections stained with MTC for collagen. The parallelism index (PI), a measure of local optical anisotropy, was calculated as $PI = (I_{MAX} - I_{MIN})/(I_{MAX} + I_{MIN})$, determined from the least-squares fit. The textural entropy parameter, a measure of pixel-level disorder, was measured using the gray-level co-occurrence matrix (GLCM) plug-in (author Julio E. Cabrera) of ImageJ (ImageJ v1.52n, NIH, Bethesda, MD). Entropy was averaged over 0, 90, 180, and 270° orientations at one-pixel offset.

2.8. Whole tumor section and histomorphometric analysis

To compare polarization signal-derived maps with conventional histological stains, tumor sections (see section 2.7, above) were imaged using an Axio Observer Z.1 microscope with motorized stage (Zeiss, Jena, Germany) and Zen software (2012, blue edition, Zeiss). Tumor cross-sectional area and aspect ratio were determined by manual line drawing around the tumor border, excluding the skin fringe, using the line drawing tool in ImageJ. Collagen area fraction within this region was determined by extracting the blue channel and setting a threshold to detect blue-stained collagen from MTC-stained sections between 76 and 254 on an 8-bit scale. This threshold excluded the blue component in the trichrome red stain (<76), determined from histogram analysis of exclusively red ROIs, and saturated background (=255). Collagen feature solidity was determined, defined as the area of each isolated binary object from blue regions in MTC-stained sections divided by the convex hull area (1 for a perfectly solid object with smooth borders, and <1 when objects have holes and undulating borders). This image feature shape descriptor was used previously to classify steatosis by grade from tissue slides of liver biopsies (Munsterman *et al* 2019), so was reasoned to be sensitive to histomorphometric alterations at a similar length scale. Differences were assessed between control and pFUS-treated tumors (n = 3 per group; 3 sections/tumor).

2.9. Statistical analysis

Processed data were presented as means $\pm$ SE. Statistical analysis was performed using GraphPad Prism v8.2.1 (GraphPad Software, San Diego, CA). An unpaired Student's t-test was used to determine statistical significance between control and pFUS groups for all experiments. Statistically significant differences were determined for $P < 0.05$. Exp. #1 (2.3): n = 10; Exp. #2 (2.5): n = 5; Exp. #3 (2.6): n = 7; Exps. #4 and 5 (2.7 and 2.8): n = 5.

3. Results

3.1. Tumor IFP measurements

In order to investigate the effects of the pFUS treatments on IFP in the tumors, we measured IFP using the wick-in-needle method, comparing untreated tumors to those treated with pFUS. Because each tumor was not identical in terms of their diameters, we normalized the location of the measurements, taken at 0.5 mm increments from the tumor surface to its center and back to the far surface, in order to be able to pool the data and carry out comparisons between the two treatment groups. The slope for the trend line generated from the measurements, was markedly lower for the pFUS treated tumors compared to the controls. The overall variability of the measurements was similarly lower for the pFUS tumors (figure 2(A)). We calculated the coefficient of variation (CV) at each measurement location, which describes the relative variability or dispersion of data in a sample in relation to the mean (i.e. the ratio of the standard deviation to the mean,
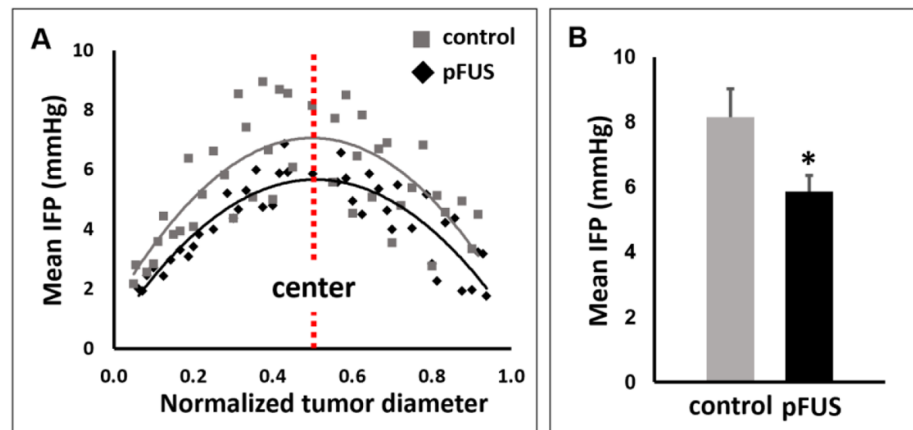
Figure 2. Results of the IFP measurements. (A) Comparisons of mean (n = 10) IFP measurements between control and pFUS treated tumors at normalized intervals (0: outer surface; 1: inner surface). A less steep gradient, from the periphery to the center, and overall lower variability, are seen for pFUS treated tumors compared to untreated controls. (B) Comparison of mean IFP in the tumor center between treatment groups. Mean IFP was 28% lower in the pFUS treated tumors compared to controls.

$CV = \delta/\mu$), allowing variability to be compared between two different data series with even substantially different means. The average *CV* for each experimental group was calculated, using the values determined at each measurement location, where the average *CV* for the pFUS treated tumors (0.15) was 42% lower than for the control tumors (0.26). The coefficient of determination (R^2) was also calculated for the slope of each group. R^2 was found to increase by 25% from 0.69 (control) to 0.86 (pFUS). The mean IFP in the core of the control tumors was 8.15 ± 0.87 mm Hg (n = 10). In the pFUS treated tumors, the mean IFP in the core was 28% lower (P = 0.04) at 5.87 ± 0.48 mm Hg (n = 10) (figure 2(B)).

3.2. *In vivo* imaging of NP delivery

In vivo imaging was used in order to determine if pFUS pretreatment of the tumors improves the overall delivery of the NPs. Epifluorescence generated by the fluorescent NPs (40 nm) was used as a surrogate metric for comparing NP delivery between the two groups. The animals were imaged live at 24 h post-administration of the NPs in both control and pFUS treated groups (figure 3(A)). Mean epifluorescence, in relative light units (RLU), in the control and pFUS treated tumors was found to be $1.67 \times 10^{10} \pm 0.45$ and $2.49 \times 10^{10} \pm 0.72$, respectively (figure 3(B)). This constituted a 49% increase in the delivery of the NPs in the pFUS treated tumors compared to the controls (P = 0.03; n = 5).
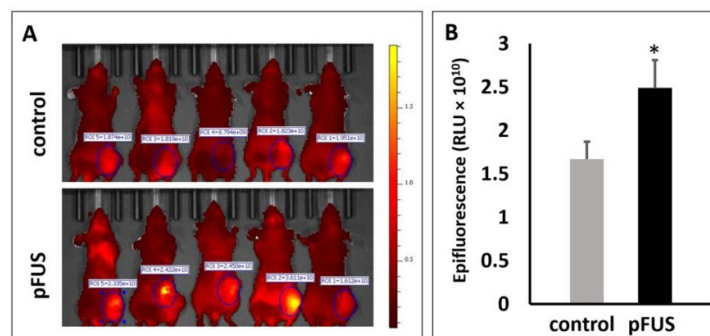
Figure 3. Effects of pFUS pretreatment on NP (40 nm) delivery. (A) *In vivo* imaging showing epifluorescent signals (pseudo-colored red) in control and pFUS treated tumors. (B) Mean epifluorescent signals in the pFUS treated tumors were 49% greater than in untreated controls (n = 5).

3.3. NP penetration and distribution

In order to determine if pFUS pretreatment also affects the penetration of the NPs into the tumors, a second group of animals was treated, and tumors were processed for fluorescence microscopy at 24 h post-administration of the NPs (200 nm). Digital images were captured of whole tumor sections which were segmented into three concentric regions for quantifying the fluorescent signal intensities (figure 4(A)). These

were presented as relative percentages to the overall signals in order to normalize and pool the data for tumors that did not possess the same diameters. In the outer third diameter region (ROI 3), the distributions were 55.8% and 45.7%, for control and pFUS treated tumors, respectively. This constituted a significant decrease of 18.1% ($P = 0.02$; n = 7) in the delivery of NPs for the pFUS treated tumors compared to controls. In the middle region (ROI 2), the percentages were 32.3% and 35.6% for control and pFUS treated tumors, respectively ($P = 0.15$; n = 7). In the most central region (ROI 1), percentages were 11.9% and 18.7% for control and pFUS treated tumors, constituting an increase of 57% in NP delivery in the pFUS treated tumors compared to the controls ($P = 0.03$; n = 7) (figure 4(B)).

Figure 4. Effects of pFUS pretreatment on NP penetration. (A) A representative tumor section indicating the three ROIs employed for quantifying the NP (200 nm) distributions (bar = 2 mm). (B) Comparison of relative NP distributions in the three ROIs for control and pFUS treated tumors (n = 7). An 18.1% decrease in NP delivery was found in the outermost region (ROI 3) in the pFUS treated tumors, compared to the control tumors. Conversely, in the innermost region (ROI 1), a 57% increase was found in the pFUS treated tumors compared to controls.

3.4. Microstructure analysis in the fibrillar collagen network

Birefringence parameter maps from pFUS-treated tumors revealed textures that were altered on the microscale compared to untreated controls (figure 5(A)). Thick bundles, red in *PI* maps, represent aligned birefringent ECM matching blue-stained fiber bundles in adjacent MTC-stained sections, while circular structures of moderate *PI* represent birefringent structures around cells, and blue regions of low *PI* represent packed tumor cells. Overall, pFUS produced a higher I_{MAX} than untreated controls (15.4 ± 10 versus 7.5 ± 3.2 on an 8-bit scale, arbitrary units; P = 0.01, n = 3) (figure 5(B)). Moreover, parameter values and texture varied spatially across the tumors, especially after pFUS treatment. In six of 14 fields-of-view pFUS-treated tumor sections had higher maximum polarization signal (figure 5(C)) and entropy (figure 5(D)) than all fields-of-view from controls. Since pFUS treatment was expected to produce microstructural alterations below the threshold of gross damage, with some spatial variation, we sought to use several parameters from birefringence maps (average I_{MAX} and *PI*, which map orientation-independent polarization signals and optical anisotropy, respectively, and entropy, a measure of pixel-level textural variation) to separate clusters of data from all fields-of-view. While the control tumors displayed more variation in *PI*, pFUS-treated tumors displayed more variation in I_{MAX} and entropy. Correlation of these parameters separated six fields-of-view acquired from all of the three pFUS-treated tumors analyzed using this approach from the other fields-of-view from the same tumors and from controls (figures 5(C) and (D), dashed lines).

3.5. Whole tumor section and histomorphometric analysis

MTC-stained sections (figures 6(A) and (B)) and Hematoxylin and Eosin-stained sections (figures 6(C) and (D)) of control (figures 6(A) and (C)) and pFUS-treated tumors (figures 6(B) and (D)) revealed a similarly intact, diffuse microstructure of collagen bundles between closely packed cells. Furthermore, employing image-based morphometric analysis, significant differences were not found between control and pFUS-treated tumors in terms of tumor cross-sectional area (figure 7(A)), collagen fiber area fraction (figure 7(B)), tumor section aspect ratio (figure 7(C)), or collagen feature solidity (figure 7(D)).

4. Discussion

Nanocarriers possess a number of advantages for delivering chemotherapeutics for the treatment of solid tumors. However, their larger size compared to the agents they encapsulate presents challenges for efficient and uniform delivery. This is attributed primarily to high IFP and the presence of fibrillar collagen in the
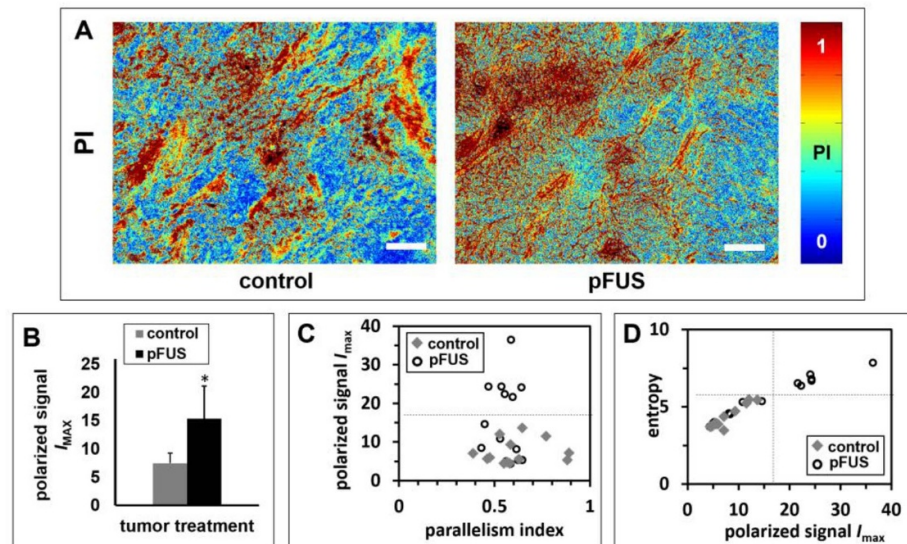
Figure 5. Effects of pFUS treatment on the microstructure of the tumor fibrillar collagen network. (A) Representative PI maps of control and pFUS treated tumors, relating to the microstructure of birefringent material in the tumors (n = 3). Differences are observed in polarized maximum signal and texture of birefringence. (B) Average polarized maximum signal, I_{MAX}, versus tumor treatment, indicating significantly greater values in pFUS treated tumors compared to controls. (C) Average polarized maximum signal, I_{MAX}, versus PI. (D) Textural entropy versus I_{MAX}. The correlation plots display variation among fields-of-view within and between groups, separated along two parameters from polarization signal maps. Separation of six fields-of-view from pFUS-treated tumors (with images from all tumors in the pFUS-treated group) was apparent from the correlation plots. Bars = 100 μm.
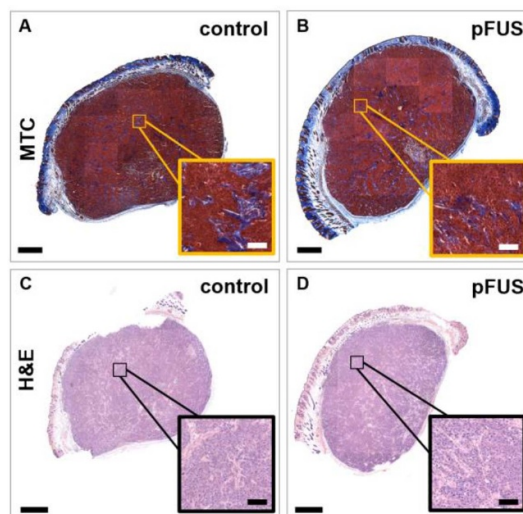
Figure 6. Effects of pFUS treatment on the histomorphology of the tumors and fibrillar collagen network. Representative (A), (B) MTC and (C), (D) H&E-stained sections of (A), (C) control and (B), (D) pFUS-treated tumors (n = 3). Insets show zoomed-in regions. No major size, structural or histomorphological differences were observed from the stained sections based on large collagen fibers or the spatial distribution of intact cells, indicating no gross tumor damage. Bars = 1 mm and 100 μm (inset).

TME (Dewhirst and Secomb 2017). Our previous studies demonstrated that pretreatment of tumors with pFUS could enhance the delivery of various therapeutic formulations (Khaibullina *et al* 2008, Poff *et al* 2008, Wang *et al* 2012, Ziadloo *et al* 2013), leading to improved treatment outcomes in terms of tumor growth inhibition (Poff *et al* 2008, Wang *et al* 2012, Ziadloo *et al* 2013). These results were associated with observations of an expanded ECS, a decrease in tissue stiffness (Ziadloo *et al* 2013), and an increase in hydraulic conductivity (Frenkel 2008b). Combined, these observations lead us to hypothesize that pFUS could be lowering IFP for improved delivery into the tumors, which motivated us to carry out the current study.

Results of our study were in agreement with many previously reported results demonstrating the spatial distribution of IFP in solid tumors xenografts. These studies consistently observed the highest IFP in the
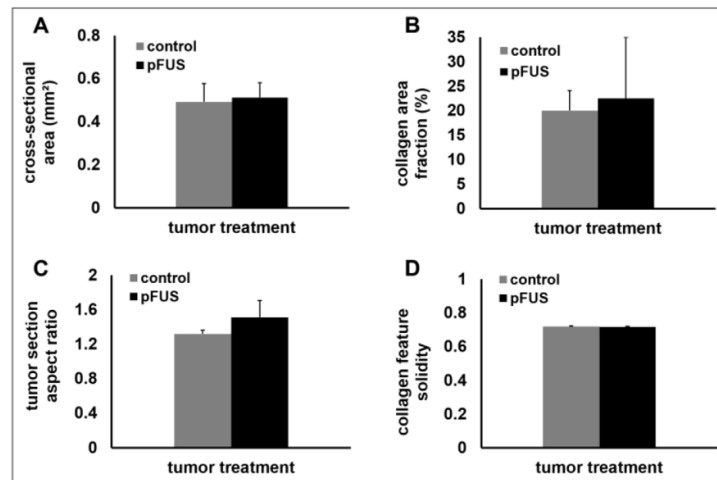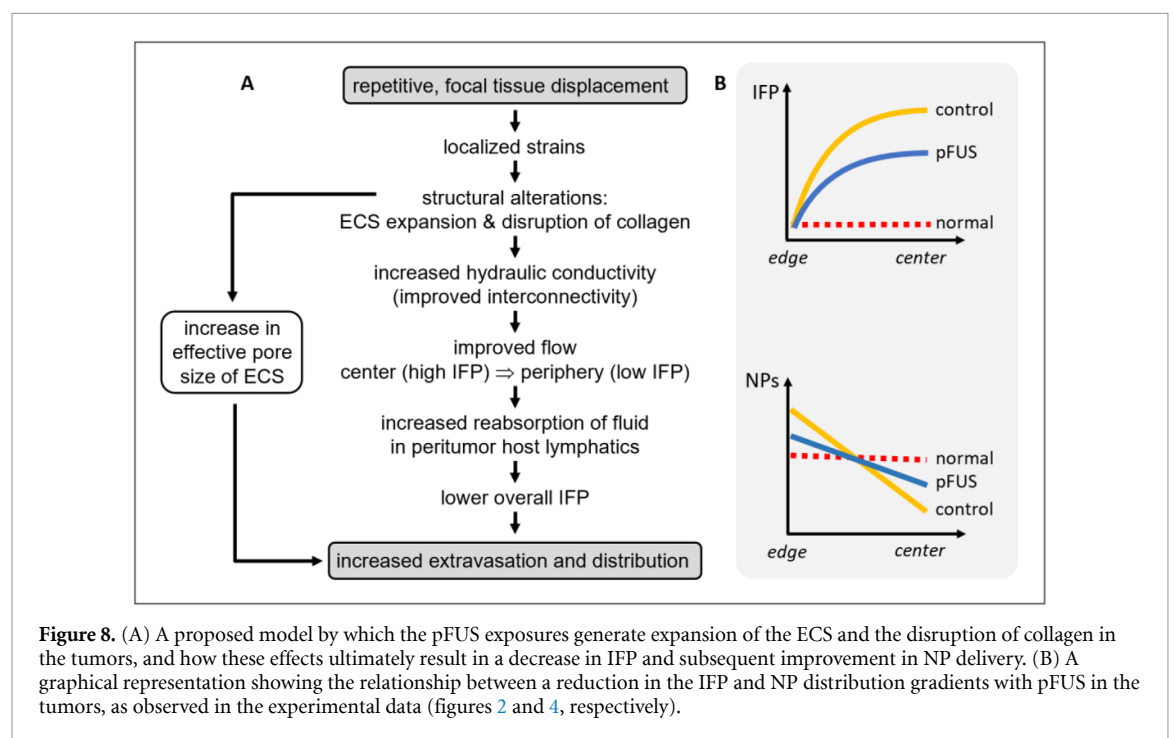
Figure 7. Whole tumor section and histomorphometric comparisons. Control and pFUS-treated tumors were compared by (A) total slide cross-sectional area, (B) collagen area fraction within the tumor section, (C) tumor section aspect ratio, and (D) collagen feature solidity within the tumor section. Statistically significant differences were not detected in any of the metrics (n = 3 tumors per group; 3 sections per tumor).

center of the tumor that decreased steeply toward the tumor periphery (Boucher *et al* 1990, Rofstad *et al* 2002, Hassid *et al* 2006). These results validated both the selection of our tumor model and the wick-in-needle device that we constructed for our investigations. In preliminary studies we determined that our tumors were not necrotic in the size range that we used in the present study (data not shown). Tumors grown with the FaDu cell line will become necrotic at larger volumes (~500 mm^3), as many tumor models do. At these larger volumes, IFP measurements were inconsistent and were at times observed to possess negative values. This, apparently, was because necrotic regions tend to present preferential routes of fluid movement (i.e. relatively greater hydraulic conductivity), drawing fluid away from regions of high pressure (Boucher *et al* 1998).

Here, we present for the first time that pretreatment of solid tumor xenografts with noninvasive pFUS can safely reduce IFP in a solid tumor xenograft model. These results were associated with an overall improvement in NP delivery, including improved delivery into the central regions of the tumors. Elevated IFP is a hallmark of solid tumors, deriving from structural abnormalities in tumor vessels, including high vascular permeability and a lack of functional lymphatics (Jain 2005). Increased IFP can reduce the pressure gradient across vessel walls, to lower the driving force for extravasation, especially for large agents such as viral vectors and nanocarriers (Heldin *et al* 2004, Jain 2005). Indeed, elevated IFP has been correlated with poor penetration of therapeutics in clinical (Gutmann *et al* 1993) and preclinical studies (Heine *et al* 2012, Winslow *et al* 2015). Our results not only showed that pFUS treatments can significantly decrease IFP in the center of the tumors, they also reduced the overall variability of the IFP measurements along the IFP gradient, from the periphery to the tumor center. Reducing heterogeneity in the TME is one of the goals of tumor modulating approaches, being associated with improved and more uniform delivery and efficacy of therapeutics for cancer therapy (Jain 2005).

Based on the results of our current and previous studies, we can present a biophysical model by which pFUS treatments lower IFP for enhancing NP delivery in solid tumors. Our previous studies demonstrated that expanding the ECS with pFUS increases the effective pore size of the tissues (Hancock *et al* 2009b, Ziadloo *et al* 2013), and as a consequence, enhances the distribution of locally administered NPs in skeletal muscle (Hancock *et al* 2009b), brain (Hersh *et al* 2016a, 2018), and solid tumor xenografts (Ziadloo *et al* 2013). Higher porosity, ε, and/or a lower wetted surface area per volume, S, could lead to higher hydraulic conductivity of the tissues, as defined by the Carman-Kozeny equation (Levick 1987). Alteration of fibrillar collagen can also affect hydraulic conductivity in tissues (Netti *et al* 2000, Mcguire *et al* 2006). Using qPLM in the current study, we observed changes in the fibrillar collagen microstructure due to pFUS treatment, which occurred on the scale of cells and between cells but not on the scale of thicker fiber bundles or whole tumor shape, and without gross structural damage to the tumor, according to analysis of MTC staining. This evidence is most consistent with a reduction of S but no change in ε leading to a larger mean hydraulic radius of flow channels (ε/S). A higher image entropy of birefringence signals indicating altered texture of birefringence, as we observed in the pFUS treated tumors, is consistent with the proposed mechanism of shear-induced pore opening by the pFUS treatments (Hancock *et al* 2009b), in which fine, isotropic collagen

network gains birefringence signal as the fibril network is deformed into parallel bundles and larger intrafibrillar spaces. Previous reports in tumor xenografts, for example, demonstrated that degradation of collagen using hyaluronidase in the interstitial matrix resulted in an increase in hydraulic conductivity (Lai-Fook *et al* 1989). Increased hydraulic conductivity, as we reported earlier using pFUS treatments (Frenkel 2008b), would improve fluid flow radially outward from regions of high pressure, normally found in the tumor center, to the periphery, where the pressure is known to be lower (Jain 1999). This would enable more fluid to be taken up by peritumor host lymphatics, since the tumors lack a functional lymphatic system (Jain 1999). As a consequence, this would lead to an overall decrease in IFP in the tumors, and ultimately contribute to better penetration and distribution of the administered agents, in addition to overall greater delivery (figure 8(A)). Indeed, we previously observed that pFUS pretreatments result in reduced stiffness in solid tumor xenografts, measured by remote elastography, as well as improved penetration and lateral distribution of locally injected NPs. When we substituted the NPs for plasmid DNA encoding for tumor necrosis factor alpha (TNFα), we observed significantly lower tumor growth rates compared to TNFα alone. These results were associated with deeper and broad regions of necrosis in the center of the tumors where the injections were administered (Ziadloo *et al* 2013).

Figure 8. (A) A proposed model by which the pFUS exposures generate expansion of the ECS and the disruption of collagen in the tumors, and how these effects ultimately result in a decrease in IFP and subsequent improvement in NP delivery. (B) A graphical representation showing the relationship between a reduction in the IFP and NP distribution gradients with pFUS in the tumors, as observed in the experimental data (figures 2 and 4, respectively).

Adjuvant treatment using antiangiogenic agents has been shown to improve chemotherapy delivery for improved tumor control (Prince *et al* 2019). These treatments are thought to normalize blood vessels in the tumors, rendering them less leaky and more organized, resulting in increased vascular function and reduced IFP for improved delivery of therapeutics and treatment efficacy (Jain 2005). Additional agents such as dexamethasone have also been shown to reduce IFP. However, these treatments were associated with an increase in blood pressure (Kristjansen *et al* 1993). In another study, hyperthermia (HT, 39.5 °C) was shown to reduce IFP as well as increase intratumoral perfusion and lower hypoxia. These treatments however were required to be applied for 4 h (Winslow *et al* 2015). In addition to requiring comparatively long treatment times, HT treatments using traditional HT modalities also suffer from the inability to provide uniform and consistent heating; especially for large tumors (Wang *et al* 2010). In the current study, the flank tumor xenografts (~250 mm^3) received four individual, two-minute pFUS treatments for a total treatment time of eight minutes.

In addition to potentially lowering IFP (Winslow *et al* 2015), HT can also generate direct effects for enhancing the delivery of NPs in solid tumor models. Enhanced NP extravasation for HT between 40 and 42 °C was shown to be temperature dependent, where treatments are required to be applied for at least 30 min. Improved results were found when increasing the treatment time to 60 min (Kong *et al* 2001). Increasing the temperature was also shown to increase the size of the NPs that are able to extravasate (Kong *et al* 2000). The proposed mechanism of HT-mediated NP delivery is thought to involve disaggregation of the endothelial cell cytoskeleton, where morphological observations appear to show the cells 'shrink'. Such

changes would be expected to increase the pore size between the cells and enable enhanced extravasation of the NPs (Kong *et al* 2001).

Our previous studies have shown that pFUS exposures typically generate temperature elevations of 4 °C–5 °C for a treatment time of 2 min. or less per treated location (Frenkel *et al* 2006, Patel *et al* 2008, O'Neill *et al* 2009). Temperature elevations such as these are capable of enhancing extravasation of NPs; however, treatment times are required to endure for at least 30 to 60 min. in order to be effective (Kong *et al* 2000, 2001). Furthermore, enhancement in NP extravasation will generally last for about 6 h until the effects are reversed (Kong *et al* 2001). In an earlier study, we provided the equivalent thermal dose produced by the pFUS exposures using a non-ultrasound source (i.e. thermal lamp). Compared to the pFUS exposures, the non-ultrasound HT treatments were not shown to enhance NP extravasation. In addition, pFUS enhancement in NP extravasation was observed to occur for greater than 24 h (O'Neill *et al* 2009). Combined, these data would suggest the absence of a thermal component for enhancement in NP extravasation using the pFUS treatments employed in the current study.

We previously proposed a novel model of ultrasound-tissue interactions, describing the manner by which pFUS exposures can generate expansion of the ECS for improving the distribution of agents in non-tumor tissue (i.e. skeletal muscle). This novel ultrasound mechanism of ECS expansion is based on a transfer of momentum from the ultrasound wave to the tissue, through the generation of unidirectional radiation forces (Lizzi *et al* 2003). The resulting displacements of tissue occurring with each pulse, and especially the shear generated at the edge of the focal zone (between regions actively and passively being displaced), create localized strains, affecting cell-to-cell interfaces and factors in the ECM to transiently and safely affect these regions and expand the ECS (Hancock *et al* 2009b). Using transmission electron microscopy (TEM), expansion of the ECS was subsequently shown to occur in a xenograft tumor model in response to pFUS, where these results were associated with improved penetration of NPs (Ziadloo *et al* 2013). In the current study, histomorphometric analysis of the tumors did not show significant differences in the collagen area fraction or collagen feature solidity, nor were differences found in the tumor cross-sectional area and aspect ratio, as result of the pFUS treatments. These results demonstrate that changes in IFP—that were associated with increased penetration and overall delivery of NPs—could safely be generated at the level of the fibrillar collagen network microstructure without affecting the overall macrostructure of the tumors. TEM analysis, required to observe expansion of the ECS as we previously demonstrated (Frenkel *et al* 2000a, 2000b, Ziadloo *et al* 2013, Hersh *et al* 2016a), was not performed in the current study.

Note, our study focused on the effects of the pFUS treatments for lowering IFP and associated increases in the delivery of NPs. We did not specifically investigate the effects on the fibrillar collagen microstructure on NP transport, which may have also contributed to improve their penetration and distribution. The effect of fibrillar collagen in the ECM of solid tumors has been well documented for limiting the penetration of therapeutic agents (Netti *et al* 2000). Degradation of fibrillar collagen in the ECM using collagenase, for example, was shown to improve the distribution of a locally administered oncolytic virus for improved tumor control. The tumors were grown in dorsal skin chambers where the effects of IFP are considered to be less pronounced (Mckee *et al* 2006). The NPs employed in the current study possessed a dense coating of PEG which limits interactions with factors in the ECM (Xu *et al* 2015). Previous studies have shown these NPs to penetrate substantially better in mucus (Kim *et al* 2013), brain parenchyma (Schneider *et al* 2015), and in solid tumors (Dancy *et al* 2016) than non-coated NPs. Despite this, we cannot rule out the potential direct contributions of the effects of pFUS on the fibrillar collagen microstructure as a contributing factor to the results presented in this study. Additional investigations will be required to differentiate between the individual contributions of pFUS on IFP and on the fibrillar collagen microstructure for enhancing NP delivery.

One of the limitations of the current study is that the pFUS effects were investigated in only one tumor model. Our previous studies, however, demonstrating the benefits of pFUS pretreatment for enhanced delivery and therapy, were shown to be consistently effective in breast (Frenkel *et al* 2006, Dromi *et al* 2007), epidermoid (Khaibullina *et al* 2008, Wang *et al* 2012), and two different head and neck (Yuh *et al* 2005, Dittmar *et al* 2005, Poff *et al* 2008, Patel *et al* 2008, Ziadloo *et al* 2013), tumor models. This is apparently due to the generic manner by which pFUS energy interacts with tumor and non-tumor tissue for generating microarchitectural changes that enhance delivery. Studies similar to the current one in other models, however, will be beneficial for future work to support the results observed herein. Furthermore, only two different NP diameters were evaluated in the current study. The smaller NPs (40 nm) were used for the *in vivo* imaging study to maximize their delivery, and the subsequent signals they generated, to best compare between the treatments. Conversely, for the study investigating the penetration of the NPs, we used larger (200 nm) NPs to minimize their penetration, as the tumor sections were being imaged with high resolution fluorescence microscopy. Based on our earlier studies, greater overall delivery of smaller NPs would have reduced the ability to more sensitively observe the effects that we found. Further studies will look at the effects

of pFUS over a larger range of NPs, to better implement and translate these treatments to the clinic. Finally, we did not carry out studies for demonstrating the reversibility of the effects generated in the TME by pFUS. These, too, will be required to further support the safety of the treatments, and will also have important implications for future clinical translation. Nevertheless, findings of the current study, taken together, extend previous therapeutic studies by determining the magnitude and profile of pFUS lowered intratumoral IFP, directly relating the mechanical alterations to NP uptake and altered birefringence signals from the tumors.

5. Conclusion

In conclusion, we demonstrate that pFUS pretreatment of solid tumors can noninvasively and nondestructively lower IFP, where these results were associated with improved penetration and overall delivery of NPs in a solid tumor xenograft model. As shown graphically (figure 8(B)), lowering of IFP and NP gradients essentially renders the TME of the tumors less heterogeneous, to more closely resemble the environment of normal (i.e. non-tumor) tissue, where IFP and the distribution of administered agents are more uniform (Jain 2005). These results support our previously reported therapeutic studies and may have implications for clinical treatments using noninvasive pFUS treatments with a range of anticancer agents for improving therapeutic outcomes.

Acknowledgments

Conflict of interest

The authors declare no conflict of interest.

ORCID iDs

Ruby N Huynh ⓘ https://orcid.org/0000-0002-2666-1013
Christopher B Raub ⓘ https://orcid.org/0000-0001-9487-0979

References

Anastasiadis P, Mohammadabadi A, Fishman M J, Smith J A, Nguyen B A, Hersh D S and Frenkel V 2019 Design, characterization and evaluation of a laser-guided focused ultrasound system for preclinical investigations *Biomed. Eng. Online* **18** 36
Boucher Y, Baxter L T and Jain R K 1990 Interstitial pressure gradients in tissue-isolated and subcutaneous tumors: implications for therapy *Cancer Res.* **50** 4478–84
Boucher Y, Brekken C, Netti P A, Baxter L T and Jain R K 1998 Intratumoral infusion of fluid: estimation of hydraulic conductivity and implications for the delivery of therapeutic agents *Br. J. Cancer* **78** 1442–8
Chen C C, Sheeran P S, Wu S Y, Olumolade O O, Dayton P A and Konofagou E E 2013 Targeted drug delivery with focused ultrasound-induced blood-brain barrier opening using acoustically-activated nanodroplets *J. Control. Release* **172** 795–804
Dancy J G, Wadajkar A S, Schneider C S, Mauban J R, Goloubeva O G, Woodworth G F, Winkles J A and Kim A J 2016 Non-specific binding and steric hindrance thresholds for penetration of particulate drug carriers within tumor tissue *J. Control. Release* **238** 139–48
Dewhirst M W and Secomb T W 2017 Transport of drugs from blood vessels to tumour tissue *Nat. Rev. Cancer* **17** 738–50
Di Paolo A and Bocci G 2007 Drug distribution in tumors: mechanisms, role in drug resistance, and methods for modification *Curr. Oncol. Rep.* **9** 109–14
Dittmar K M, Xie J, Hunter F, Trimble C, Bur M, Frenkel V and Li K C 2005 Pulsed high-intensity focused ultrasound enhances systemic administration of naked DNA in squamous cell carcinoma model: initial experience *Radiology* **235** 541–6
Dreher M R, Liu W, Michelich C R, Dewhirst M W, Yuan F and Chilkoti A 2006 Tumor vascular permeability, accumulation, and penetration of macromolecular drug carriers *J. Natl. Cancer Inst.* **98** 335–44
Dromi S *et al* 2007 Pulsed-high intensity focused ultrasound and low temperature-sensitive liposomes for enhanced targeted drug delivery and antitumor effect *Clin. Cancer Res.* **13** 2722–7
Elmghirbi R, Nagaraja T N, Brown S L, Keenan K A, Panda S, Cabral G, Bagher-Ebadian H, Divine G W, Lee I Y and Ewing J R 2018 Toward a noninvasive estimate of interstitial fluid pressure by dynamic contrast-enhanced MRI in a rat model of cerebral tumor *Magn. Reson. Med* **80** 2040–52 .
Focused Ultrasound Foundation *Diseases and Conditions: Overview* (available at: https://www.fusfoundation.org/diseases-and-conditions-all/overview)
Frenkel V 2008a Ultrasound mediated delivery of drugs and genes to solid tumors *Adv. Drug Deliv. Rev.* **60** 1193–208
Frenkel V 2008b Pulsed-high intensity focused ultrasound (HIFU) exposures for enhanced delivery of therapeutics: mechanisms and applications *AIP Conf. Proc.* **829** 528–32

Frenkel V, Etherington A, Greene M, Quijano J, Xie J, Hunter F, Dromi S and Li K C 2006 Delivery of liposomal doxorubicin (Doxil) in a breast cancer tumor model: investigation of potential enhancement by pulsed-high intensity focused ultrasound exposure *Acad. Radiol.* **13** 469–79

Frenkel V, Kimmel E and Iger Y 2000a Ultrasound-facilitated transport of silver chloride (AgCl) particles in fish skin *J. Control. Release* **68** 251–61

Frenkel V, Kimmel E and Iger Y 2000b Ultrasound-induced intercellular space widening in fish epidermis *Ultrasound Med. Biol.* **26** 473–80

Galmarini C M and Galmarini F C 2003 Multidrug resistance in cancer therapy: role of the microenvironment *Curr. Opin. Invest. Drugs* **4** 1416–21

Gutmann R, Leunig A, Leunig M and Feyh J 1993 Importance of increased interstitial fluid pressure in therapy of malignant tumors of the head-neck area *Laryngorhinootologie* **72** 338–41

Gutmann R, Leunig M, Feyh J, Goetz A E, Messmer K, Kastenbauer E and Jain R K 1992 Interstitial hypertension in head and neck tumors in patients: correlation with tumor size *Cancer Res.* **52** 1993–5

Hancock H, Dreher M R, Crawford N, Pollock C B, Shih J, Wood B J, Hunter K and Frenkel V 2009a Evaluation of pulsed high intensity focused ultrasound exposures on metastasis in a murine model *Clin. Exp. Metastasis* **26** 729–38

Hancock H A, Smith L H, Cuesta J, Durrani A K, Angstadt M, Palmeri M L, Kimmel E and Frenkel V 2009b Investigations into pulsed high-intensity focused ultrasound-enhanced delivery: preliminary evidence for a novel mechanism *Ultrasound Med. Biol.* **35** 1722–36

Harrington K J, Rowlinson-Busza G, Syrigos K N, Vile R G, Uster P S, Peters A M and Stewart J S 2000a Pegylated liposome-encapsulated doxorubicin and cisplatin enhance the effect of radiotherapy in a tumor xenograft model *Clin. Cancer Res.* **6** 4939–49

Harrington K J, Rowlinson-Busza G, Uster P S and Stewart J S 2000b Pegylated liposome-encapsulated doxorubicin and cisplatin in the treatment of head and neck xenograft tumours *Cancer Chemother. Pharmacol.* **46** 10–18

Hassid Y, Furman-Haran E, Margalit R, Eilam R and Degani H 2006 Noninvasive magnetic resonance imaging of transport and interstitial fluid pressure in ectopic human lung tumors *Cancer Res.* **66** 4159–66

Heine M, Freund B, Nielsen P, Jung C, Reimer R, Hohenberg H, Zangemeister-Wittke U, Wester H J, Luers G H and Schumacher U 2012 High interstitial fluid pressure is associated with low tumour penetration of diagnostic monoclonal antibodies applied for molecular imaging purposes *PLoS ONE* **7** e36258

Heldin C H, Rubin K, Pietras K and Ostman A 2004 High interstitial fluid pressure—an obstacle in cancer therapy *Nat. Rev. Cancer* **4** 806–13

Hersh D S *et al* 2018 MR-guided transcranial focused ultrasound safely enhances interstitial dispersion of large polymeric nanoparticles in the living brain *PLoS ONE* **13** e0192240

Hersh D S, Nguyen B A, Dancy J G, Adapa A R, Winkles J A, Woodworth G F, Kim A J and Frenkel V 2016a Pulsed ultrasound expands the extracellular and perivascular spaces of the brain *Brain Res.* **1646** 543–50

Hersh D S, Wadajkar A S, Roberts N B, Perez J G, Connolly N P, Frenkel V, Winkles J A, Woodworth G F and Kim A J 2016b Evolving drug delivery strategies to overcome the blood brain barrier *Curr. Pharm. Des.* **22** 1177–93

Hynynen K, Mcdannold N, Sheikov N A, Jolesz F A and Vykhodtseva N 2005 Local and reversible blood-brain barrier disruption by noninvasive focused ultrasound at frequencies suitable for trans-skull sonications *Neuroimage* **24** 12–20

Jain R K 1999 Transport of molecules, particles, and cells in solid tumors *Annu. Rev. Biomed. Eng.* **1** 241–63

Jain R K 2005 Normalization of tumor vasculature: an emerging concept in antiangiogenic therapy *Science* **307** 58–62

Kennedy J E 2005 High-intensity focused ultrasound in the treatment of solid tumours *Nat. Rev. Cancer* **5** 321–7

Khaibullina A, Jang B S, Sun H, Le N, Yu S, Frenkel V, Carrasquillo J A, Pastan I, Li K C and Paik C H 2008 Pulsed high-intensity focused ultrasound enhances uptake of radiolabeled monoclonal antibody to human epidermoid tumor in nude mice *J. Nucl. Med.* **49** 295–302

Kim A J *et al* 2013 Use of single-site-functionalized PEG dendrons to prepare gene vectors that penetrate human mucus barriers *Angew. Chem. Int. Ed. Engl.* **52** 3985–8

Kong G, Braun R D and Dewhirst M W 2000 Hyperthermia enables tumor-specific nanoparticle delivery: effect of particle size *Cancer Res.* **60** 4440–5

Kong G, Braun R D and Dewhirst M W 2001 Characterization of the effect of hyperthermia on nanoparticle extravasation from tumor vasculature *Cancer Res.* **61** 3027–32

Kristjansen P E, Boucher Y and Jain R K 1993 Dexamethasone reduces the interstitial fluid pressure in a human colon adenocarcinoma xenograft *Cancer Res.* **53** 4764–6

Lai-Fook S J, Rochester N L and Brown L V 1989 Effects of albumin, dextran, and hyaluronidase on pulmonary interstitial conductivity *J. Appl. Physiol.* **67** 606–13

Levick J R 1987 Flow through interstitium and other fibrous matrices *Q. J. Exp. Physiol.* **72** 409–37

Li K, Correa S O, Pham P, Raub C B and Luo X 2017 Birefringence of flow-assembled chitosan membranes in microfluidics *Biofabrication* **9** 034101

Lizzi F L, Muratore R, Deng C X, Ketterling J A, Alam S K, Mikaelian S and Kalisz A 2003 Radiation-force technique to monitor lesions during ultrasonic therapy *Ultrasound Med. Biol.* **29** 1593–605

Mcdonald D M and Choyke P L 2003 Imaging of angiogenesis: from microscope to clinic *Nat. Med.* **9** 713–25

Mcguire S, Zaharoff D and Yuan F 2006 Nonlinear dependence of hydraulic conductivity on tissue deformation during intratumoral infusion *Ann. Biomed. Eng.* **34** 1173–81

Mckee T D, Grandi P, Mok W, Alexandrakis G, Insin N, Zimmer J P, Bawendi M G, Boucher Y, Breakefield X O and Jain R K 2006 Degradation of fibrillar collagen in a human melanoma xenograft improves the efficacy of an oncolytic herpes simplex virus vector *Cancer Res.* **66** 2509–13

Mow V C, Mak A F, Lai W M, Rosenberg L C and Tang L H 1984 Viscoelastic properties of proteoglycan subunits and aggregates in varying solution concentrations *J. Biomech.* **17** 325–38

Munsterman I D, van Erp M, Weijers G, Bronkhorst C, de Korte C L, Drenth J P H, van der Laak J and Tjwa E 2019 A novel automatic digital algorithm that accurately quantifies steatosis in NAFLD on histopathological whole-slide images *Cytometry B Clin. Cytom.* **96** 521–8

Nance E A, Woodworth G F, Sailor K A, Shih T Y, Xu Q, Swaminathan G, Xiang D, Eberhart C and Hanes J 2012 A dense poly(ethylene glycol) coating improves penetration of large polymeric nanoparticles within brain tissue *Sci. Transl. Med.* **4** 149ra119

Netti P A, Berk D A, Swartz M A, Grodzinsky A J and Jain R K 2000 Role of extracellular matrix assembly in interstitial transport in solid tumors *Cancer Res.* **60** 2497–503

O'Neill B E, Vo H, Angstadt M, Li K P, Quinn T and Frenkel V 2009 Pulsed high intensity focused ultrasound mediated nanoparticle delivery: mechanisms and efficacy in murine muscle *Ultrasound Med. Biol.* **35** 416–24

Patel P R, Luk A, Durrani A, Dromi S, Cuesta J, Angstadt M, Dreher M R, Wood B J and Frenkel V 2008 *In vitro* and *in vivo* evaluations of increased effective beam width for heat deposition using a split focus high intensity ultrasound (HIFU) transducer *Int. J. Hypertherm.* **24** 537–49

Plummer R *et al* 2011 A Phase I clinical study of cisplatin-incorporated polymeric micelles (NC-6004) in patients with solid tumours *Br. J. Cancer* **104** 593–8

Poff J A, Allen C T, Traughber B, Colunga A, Xie J, Chen Z, Wood B J, Van Waes C, Li K C and Frenkel V 2008 Pulsed high-intensity focused ultrasound enhances apoptosis and growth inhibition of squamous cell carcinoma xenografts with proteasome inhibitor bortezomib *Radiology* **248** 485–91

Prince A C, Patel N G, Moore L S, Mcgee A S, Ahn J C, Willey C D, Carroll W R, Rosenthal E L and Warram J M 2019 Adjuvant anti-angiogenic therapy enhances chemotherapeutic uptake in a murine model of head and neck cancer *J. Drug Target* **27** 193–200

Ranjan A *et al* 2012 Image-guided drug delivery with magnetic resonance guided high intensity focused ultrasound and temperature sensitive liposomes in a rabbit Vx2 tumor model *J. Control. Release* **158** 487–94

Rieppo J, Hallikainen J, Jurvelin J S, Kiviranta I, Helminen H J and Hyttinen M M 2008 Practical considerations in the use of polarized light microscopy in the analysis of the collagen network in articular cartilage *Microsc. Res. Tech.* **71** 279–87

Rofstad E K, Tunheim S H, Mathiesen B, Graff B A, Halsor E F, Nilsen K and Galappathi K 2002 Pulmonary and lymph node metastasis is associated with primary tumor interstitial fluid pressure in human melanoma xenografts *Cancer Res.* **62** 661–4

Schneider C S, Perez J G, Cheng E, Zhang C, Mastorakos P, Hanes J, Winkles J A, Woodworth G F and Kim A J 2015 Minimizing the non-specific binding of nanoparticles to the brain enables active targeting of Fn14-positive glioblastoma cells *Biomaterials* **42** 42–51

Snipstad S *et al* 2017 Ultrasound improves the delivery and therapeutic effect of nanoparticle-stabilized microbubbles in breast cancer xenografts *Ultrasound Med. Biol.* **43** 2651–69

Uchino H, Matsumura Y, Negishi T, Koizumi F, Hayashi T, Honda T, Nishiyama N, Kataoka K, Naito S and Kakizoe T 2005 Cisplatin-incorporating polymeric micelles (NC-6004) can reduce nephrotoxicity and neurotoxicity of cisplatin in rats *Br. J. Cancer* **93** 678–87

Wang S *et al* 2012 Pulsed high intensity focused ultrasound increases penetration and therapeutic efficacy of monoclonal antibodies in murine xenograft tumors *J. Control. Release* **162** 218–24

Wang S, Zderic V and Frenkel V 2010 Extracorporeal, low-energy focused ultrasound for noninvasive and nondestructive targeted hyperthermia *Future Oncol.* **6** 1497–511

Wang Y and Yuan F 2006 Delivery of viral vectors to tumor cells: extracellular transport, systemic distribution, and strategies for improvement *Ann. Biomed. Eng.* **34** 114–27

Winslow T B, Eranki A, Ullas S, Singh A K, Repasky E A and Sen A 2015 A pilot study of the effects of mild systemic heating on human head and neck tumour xenografts: analysis of tumour perfusion, interstitial fluid pressure, hypoxia and efficacy of radiation therapy *Int. J. Hypertherm.* **31** 693–701

Xu Q *et al* 2015 Impact of surface polyethylene glycol (PEG) density on biodegradable nanoparticle transport in Mucus *ex vivo* and distribution *in vivo* *ACS Nano* **9** 9217–27

Yuh E L, Shulman S G, Mehta S A, Xie J, Chen L, Frenkel V, Bednarski M D and Li K C 2005 Delivery of systemic chemotherapeutic agent to tumors by using focused ultrasound: study in a murine model *Radiology* **234** 431–7

Ziadloo A, Xie J and Frenkel V 2013 Pulsed focused ultrasound exposures enhance locally administered gene therapy in a murine solid tumor model *J. Acoust. Soc. Am.* **133** 1827–34

Znati C A, Rosenstein M, Boucher Y, Epperly M W, Bloomer W D and Jain R K 1996 Effect of radiation on interstitial fluid pressure and oxygenation in a human tumor xenograft *Cancer Res.* **56** 964–8